

**Kinetic electronic excitation of solids by fast-particle bombardment**Stefan Meyer,<sup>1,3</sup> Christian Heuser,<sup>1</sup> Detlef Diesing,<sup>2</sup> and Andreas Wucher<sup>1,\*</sup><sup>1</sup>*Fachbereich Physik, Universität Duisburg-Essen, 47048 Duisburg, Germany*<sup>2</sup>*Fachbereich Chemie, Universität Duisburg-Essen, 45117 Essen, Germany*<sup>3</sup>*Carl Zeiss AG, 73447 Oberkochen, Germany*

(Received 20 May 2008; revised manuscript received 17 June 2008; published 16 July 2008)

The kinetic excitation of hot electrons and conduction-band vacancies following the impact of an energetic particle onto a solid surface was studied using metal-insulator-metal tunnel junctions. The top metal layer (polycrystalline silver) was bombarded by charged and neutral Ar projectiles of kinetic energies between 1 and 15 keV. Hot charge carriers generated within the collision cascade initiated by the projectile impact were detected as a tunneling current across the oxide barrier into the underlying substrate metal electrode. The tunneling yield is shown to depend monotonously on the kinetic impact energy with no notable contribution of potential emission. The dependence, however, is different for singly charged and neutral projectiles. Applying a bias voltage between the two metal electrodes, information about the energy spectrum of the excited carriers is obtained. The experimental data are interpreted in terms of a simple two-temperature tunneling model, yielding a kinetically induced transient electron “temperature” on the order of  $10^4$  K.

DOI: [10.1103/PhysRevB.78.035428](https://doi.org/10.1103/PhysRevB.78.035428)

PACS number(s): 79.20.Rf, 34.35.+a, 73.40.Rw, 79.90.+b

**I. INTRODUCTION**

If a surface is bombarded with energetic particles, the imparted kinetic energy is dissipated within the underlying solid. The energy loss (“stopping”) of the projectile may in principle be mediated either by interaction with target electrons (“electronic stopping”) or atoms (“nuclear stopping”).<sup>1</sup> Nuclear stopping proceeds by a series of mostly elastic collisions, where target atoms are set in motion and may undergo further collisions with other target atoms. Shortly (subps) after the impact, part of the dissipated energy is therefore stored in a collision cascade,<sup>2</sup> both in the form of kinetic and potential energy of the projectile and recoiling atoms. As a consequence, surface atoms may be ejected into the vacuum, a process which is called “sputtering.”<sup>3</sup> Another part of the dissipated energy is transferred to the electronic subsystem of the solid, leading to a transient local electronic excitation at or near the bombarded surface. In general, these excitations manifest in the creation of hot electrons in energetic states located above the Fermi level. Since each excitation of a hot electron leaves a vacancy in an originally filled state below the Fermi level, kinetic excitation will also produce a distribution of conduction-band vacancies (defect electrons), which will in the following be referred to as “holes.”<sup>4</sup> If some electrons gain enough energy to overcome the surface work function, they may be released into the vacuum. This process is called “kinetic electron emission”<sup>5</sup> and will in the following also be referred to as “external emission.” Electrons in states located below the vacuum level, on the other hand, cannot be emitted and remain inside the solid, where they may undergo further interactions with other electrons, atoms or phonons. As a consequence, the excitation will spread inside the solid, away from the point where it was originally created, until the system finally thermalizes.

Kinetic electron emission has been studied extensively in the past, both experimentally and theoretically, and the results have been reviewed on several occasions.<sup>5,6</sup> In particular, a wealth of experimental data exist on yields and energy

spectra of the emitted electrons.<sup>6</sup> It is generally found that the yield, i.e., the average number of electrons released per projectile impact, increases monotonically with impact energy or velocity of the projectile. Many experiments have found a linear dependence on impact velocity, but there are also exceptions to this general rule.<sup>5-7</sup> From the theoretical perspective, practically all models published so far predict the electron yield to be proportional to the electronic stopping power  $S_e$  experienced by the projectile immediately upon entrance into the solid, i.e., at its original kinetic impact energy.<sup>8,9</sup> In the keV energy range of interest here,  $S_e$  is roughly proportional to the particle velocity,<sup>10</sup> thus leading to the often observed linear yield dependence. Energy spectra of emitted electrons generally feature maxima in the eV range, with extended tails toward high energies.<sup>5</sup> The low average emission energy has been attributed to both the original excitation spectrum generated by the moving particle<sup>11-13</sup> and the generation of low-energy secondary electrons by electron-electron collisions.<sup>9</sup>

To date, only very little experimental information exists on kinetically induced low-energy electronic excitations. However, in view of the fact that calculated excitation spectra are dominated by low-energy excitations,<sup>11</sup> it appears highly desirable to obtain information on the population of states that are located below the vacuum level, which cannot be studied by external electron emission. We have recently demonstrated that these “hot” internal electrons can be detected by means of a buried tunnel junction located at depths on the order of 10 nm below the surface.<sup>14</sup> In this type of experiments, the junction is realized in the form of a metal-insulator-metal (MIM) film structure, where the upper metal layer represents the actual target, the surface of which is bombarded with energetic projectiles. A thin oxide layer then acts as a tunneling barrier between the top target metal film and the metal substrate below. The idea is that electrons in states located above the Fermi level can overcome the barrier and are then detected as a tunneling current into the metal substrate. In principle, both the height and the thickness of the barrier can be controlled via the preparation of the insu-

lating film. Moreover, it is possible to apply a bias voltage between both metal layers, thus modifying the shape of the potential barrier across the junction in the course of one experiment. As shown below, both features open the possibility to gain information about the energy spectrum of excited electrons generated by kinetic excitation processes.

The applicability of MIM junctions for the detection of hot internal electrons has been demonstrated earlier.<sup>15</sup> Originally, the technique had been developed in order to investigate the injection of hot charge carriers into metallic surfaces by means of chemical surface reactions.<sup>16,17</sup> The application for kinetically excited electrons was demonstrated in our earlier publications.<sup>14,18</sup> The present work expands on these studies by investigating the dependence of the internal electron emission yields on parameters like the thickness of the top target metal layer as well as the kinetic impact energy and charge state of the projectiles. In order to evaluate the effects induced by the projectile charge state, the primary ions were neutralized in a gas cell, and the resulting flux of neutral projectiles was monitored using the sputtering process. This is possible, since it is well known that the sputter yield of a metallic surface is not influenced by the projectile charge state.<sup>19</sup> In an effort to characterize the spectrum of the kinetic excitation, the dependence of the internal electron emission yield on a bias voltage across the tunnel junction was studied, and the results are discussed in terms of a simple two-temperature tunneling model simulating the measured data.

## II. EXPERIMENT

### A. General setup

The experiments were carried out in an ultrahigh vacuum (UHV) system with a base pressure of about  $10^{-9}$  mbar. The projectiles were generated by an ion gun delivering a focused and pulsed rare-gas beam with energies reaching from 1 to 15 keV and a current of a few hundred nA. The projectiles impinge onto the bombarded surface under  $45^\circ$  with respect to the surface normal. In general, the target was realized in the form of the top metal layer of a MIM structure. The bombardment induced tunneling current was measured in dependence of the bias voltage applied across the tunnel junction by means of a programmable potentiostat in connection with a sensitive current-to-voltage converter. In order to determine the influence of the projectile charge state, the ion source was retrofitted with a home-built neutralizer based on a charge-exchange gas cell. The neutral projectile flux onto the sample surface was monitored by sputtered neutral mass spectrometry (SNMS), i.e., neutral atoms released from the bombarded surface by either charged or neutral projectile impact were detected by a time-of-flight mass spectrometer equipped with a pulsed excimer laser for single-photon postionization.<sup>20,21</sup> In these experiments, the MIM target was replaced by a polycrystalline indium sample, since the lower ionization potential of In atoms (5.78 eV vs 7.57 eV for Ag<sup>21</sup>) allows single-photon ionization with UV radiation of 6.4 eV photon energy readily available from a conventional ArF excimer laser.

### B. Projectile source

The projectile beam was generated by means of a commercial ion source (Atomika Microfocus, cold cathode version) delivering mass selected rare-gas ions of kinetic energies between 1 and 15 keV. The way it is operated in our instrument, this source typically produces a beam of 10-keV Ar<sup>+</sup> ions with a current of 300 nA into a spot size of either 500  $\mu\text{m}$  or 2 mm diameter [full width at half maximum (FWHM)], depending on whether the objective lens is used or not. For generation of neutral projectiles, the source was retrofitted with a charge-exchange gas cell which could be filled with argon up to a pressure of about  $10^{-2}$  mbar. The cell was realized in the form of a tube of 3 mm inner diameter and 80 mm length, with the gas being introduced into the center of the tube. During operation with neutral projectiles, the remaining ions were deflected out of the beam by means of two blanking plates located at the end of the tube.

During their passage across the neutralizer, the projectile ions can either undergo resonant charge-exchange or elastic-scattering collisions with thermal gas atoms. While the former neutralize a projectile ion without significantly changing its trajectory, the latter lead to a pressure dependent modification of the spatial beam shape, which manifests as a reduction of the useful projectile flux at the target surface. Both charged and neutral projectiles lead to the detection of a mass spectrometric SNMS signal of neutral In atoms sputtered from the indium target, which is directly proportional to the projectile flux. With the deflection voltage in the primary beam switched off, both ions and neutrals can reach the target and induce SNMS signals  $S_i$  and  $S_n$ , respectively. With the deflection voltage switched on, only the neutral projectiles can still generate a signal  $S_n$ . With the assumption that elastic-scattering losses are the same for ionic and neutral projectiles, the neutralization efficiency can be readily determined from the SNMS signal ratio

$$\eta(p) = \frac{S_n(p)}{S_n(p) + S_i(p)} \quad (1)$$

as a function of the gas pressure  $p$ . This dependence is shown in Fig. 1. It is seen that neutralization efficiencies larger than 90% can be reached at a gas pressure of about  $4 \times 10^{-7}$  mbar in the analysis chamber. The data can be fitted to the theoretical expectation

$$\eta(p) = [1 - \exp(-a\sigma_n p_{\text{cell}})], \quad (2)$$

where  $a=2 \times 10^{21}(\text{mbar m}^2)^{-1}$  is a factor determined from the geometrical properties of the neutralizer,  $p_{\text{cell}}$  is the pressure in the gas cell (which is proportional to the pressure  $p$  measured in the analysis chamber), and  $\sigma_n$  denotes the neutralization cross section. The respective fitting curves have been included in Fig. 1. Obviously, the neutralization cross section slightly depends on the projectile energy, becoming larger with increasing energy. A more detailed discussion of the neutralization data will be published elsewhere.<sup>22</sup> For the purpose of the present paper, it is essential that the ratio  $S_n/S_i$  reflects the ratio between neutral and ionized projectile fluxes. In connection with the measured ion current, this al-

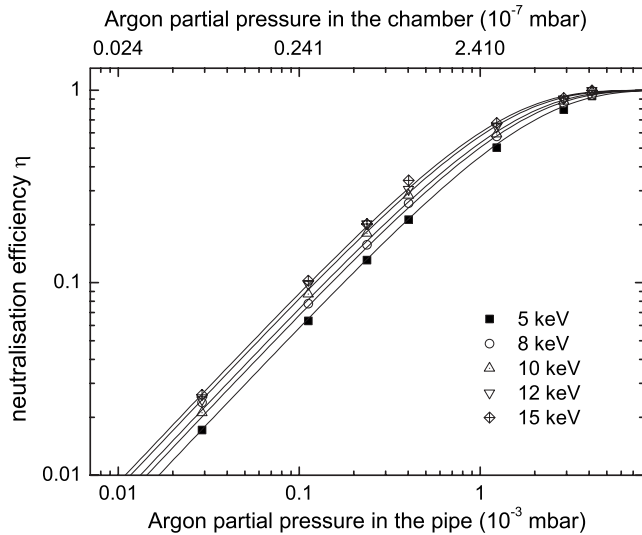


FIG. 1. Neutralization efficiency of  $\text{Ar}^+$  projectile ions vs Ar gas pressure in the cell (lower axis) or in the analysis chamber (upper axis), respectively.

lows to unambiguously determine the flux of neutral projectiles impinging onto the target surface.

**C. Metal-insulator-metal structures**

As outlined above, the bombarded sample is realized as the top metal layer of a MIM structure. The MIM junctions were produced by first vapor depositing a polycrystalline aluminum electrode of 40–50 nm thickness onto an insulating glass substrate in a high-vacuum ( $\sim 5 \times 10^{-8}$  mbar) environment. In a second step, the sample was removed from the vacuum system and the aluminum was locally oxidized to form an amorphous  $\text{AlO}_x$  overlayer of about 3 nm thickness. Details of the electrochemical treatment employed to ensure an extremely homogenous oxide film are described elsewhere<sup>23</sup> and will not be repeated here. In a third step, the sample was reintroduced into vacuum, and a polycrystalline silver layer was vapor deposited on top of the oxide layer.

For this purpose, the UHV system was equipped with a preparation chamber equipped with an electron beam evaporator and a quartz crystal deposition monitor.

In choosing the thickness of the top metal film, several aspects need to be considered. First, the excited electrons need to be generated close enough to the metal-oxide interface in order to be able to reach and pass the barrier without losing their energy in secondary collisions with other electrons. This leads to the requirement that the top layer needs to be as thin as possible, with its thickness at maximum being comparable to the average ballistic mean-free path of the excited charge carriers. On the other hand, energetic projectiles may penetrate the surface and generate defects in the oxide layer. For the specific case of silver as a top metal, computer simulations using the Monte Carlo code SRIM2006 (Refs. 24 and 25) reveal a mean range of about 6 nm for 10-keV Ar impinging under  $45^\circ$ . This, of course, imposes a lower limit for the top layer thickness, since it must be avoided that the oxide layer is modified strongly enough to alter the electrical properties of the tunnel junction. As a consequence of these considerations, we chose a top metal film thickness of 20 nm as the nominal value for the experiments performed here.

Both substrate and top metal layers were laterally shaped in the form of stripes of 2 mm width and oriented perpendicular to each other, thus limiting the electrically active tunneling junction to the overlap area of  $2 \times 2 \text{ mm}^2$ . For the experiments involving neutral projectiles, this area was increased to  $5 \times 5 \text{ mm}^2$  in order to accommodate the larger spatial width of the neutral beam. During deposition, the electrical resistance of both films was monitored. Deposition was performed at low temperature ( $\sim 130 \text{ K}$ ) in order to improve the lateral homogeneity and monitor the annealing of the film during subsequent heating to room temperature. Figure 2 shows the specific resistance both as a function of film thickness during deposition (a) and of temperature during warm-up after deposition (b). In contrast to the behavior of bulk silver, the resistance is seen to decrease with increasing temperature, since the annealing effect acts to homogenize the deposited film. Ultimately, at a film thickness of about 11 nm a resistance of about 2.5 times the value of solid

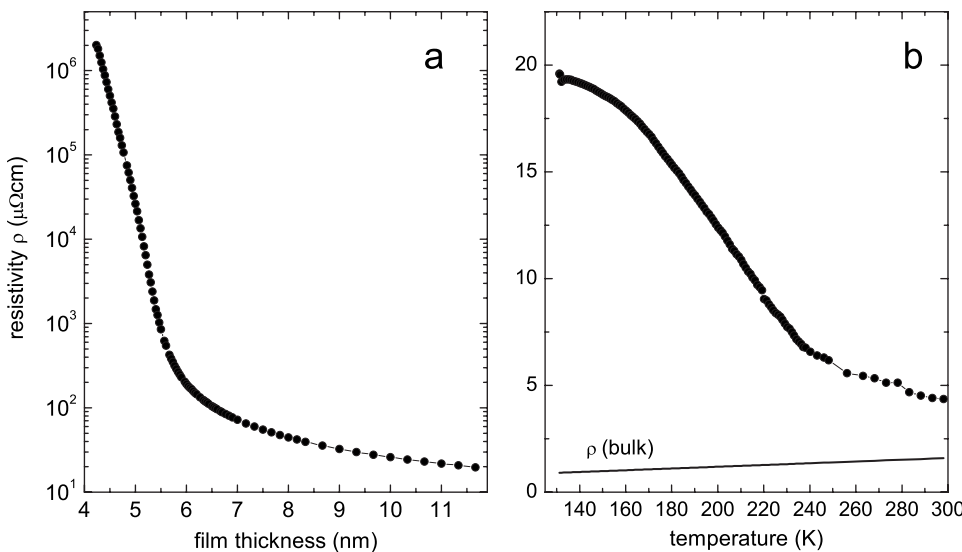


FIG. 2. Specific resistance of the silver cover electrode (a) vs film thickness during low-temperature deposition and (b) vs temperature during warm-up of final film of 11.6 nm thickness. Solid line: resistance of bulk solid silver.

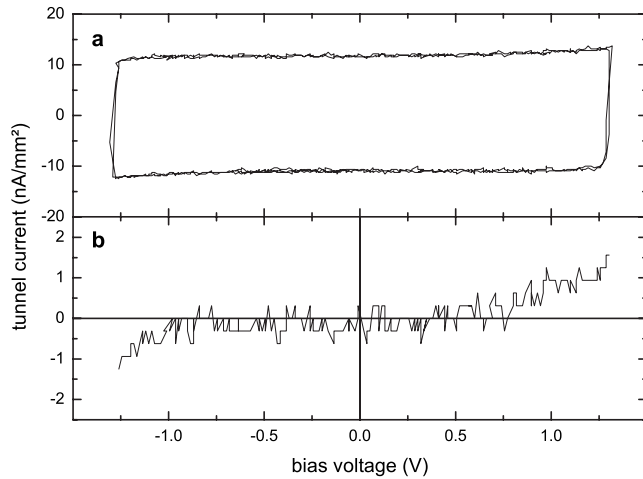


FIG. 3. Tunneling current across the MIM junction vs applied bias voltage (a) measured dynamically with a voltage ramp of 500 mV/s and (b) measured statically.

silver is reached. Note that the data displayed in Fig. 2(b) closely resemble those measured by Luo *et al.*<sup>26</sup> for low-temperature deposition and annealing of Ag on a 24-nm silver layer.

The electrical properties of the MIM were examined by measuring the tunneling current across the junction as a function of the bias voltage between the two metal electrodes. This was done by applying a voltage ramp on the order of 500 mV/s by means of a programmable potentiostat. A typical  $I$ - $V$  characteristic measured this way is depicted in Fig. 3(a). The vertical shift between the upper and lower branches of the curve is produced by the charging dynamics of the capacitor represented by the tunnel junction. Normalizing the charging current to the scan speed and the junction area reveals a capacitance of about 20 nF/mm<sup>2</sup>, which was virtually the same for all MIM structures used in this work. This finding is important since it illustrates the reproducibility of the quality and thickness of the oxide film. If the dynamic effect is eliminated from the data [Fig. 3(b)], an exponential  $I$ - $V$  dependence is found which is typical for a tunnel junction. In order to eliminate possible differences between the electrical properties of different MIM structures, only measurements performed using the same device were used for quantitative data comparison. In addition, the  $I$ - $V$  curve of every MIM junction was frequently checked throughout each data acquisition series, and the device was discarded if a significant change was detected.

### III. RESULTS AND DISCUSSION

The main goal of the present work is to investigate the dissipation channels of kinetic energy imparted to a solid surface via fast-particle bombardment. Particular emphasis is put on the short-time energy transfer into electronic degrees of freedom. The resulting excitation is studied via the detection of hot charge carriers generated by the particle kinetics initiated by the projectile impact. For that purpose, MIM tunnel junctions are employed, where the first metal layer represents the actual bombarded target, while the insulating

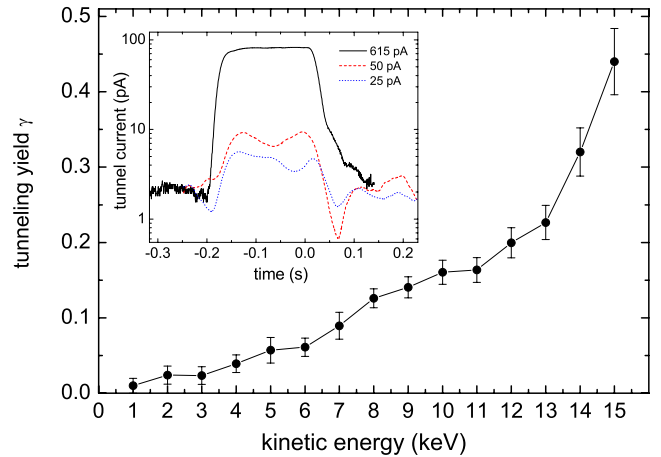


FIG. 4. (Color online) Tunneling yield as a function of the kinetic impact energy of Ar<sup>+</sup> ions bombarding the polycrystalline top silver electrode of a MIM device. Inset: Pulse response of measured tunneling current to the primary ion pulse at three different values of the (dc) primary ion current.

oxide film acts as a tunneling barrier for the generated hot carriers. The bombardment induced electronic excitation then manifests as a tunneling current into the underlying substrate layer.

This section is organized as follows: First, we demonstrate in Sec. III A that it is possible to detect a measurable bombardment induced tunneling current and define the tunneling yield  $\gamma$ . In Sec. III B, we investigate the dependence of this quantity on the projectile impact energy and demonstrate that the detected excitation is indeed arising from kinetic effects. In Sec. III C, the role of the potential (ionization) energy of projectile ions is investigated by studying the dependence of  $\gamma$  on the projectile charge state. Section III D describes the dependence of tunneling yields on the film thickness of the topmost (excited) metal layer. Finally, the influence of a bias voltage applied between the two metal electrodes of the MIM structure is described and discussed in Secs. III E and III F.

#### A. Tunneling yield

The bombardment induced tunneling current is determined from the pulse response of the measured MIM current to the pulsed projectile ion beam. In order to illustrate the sensitivity, an example is shown in the inset of Fig. 4, which was obtained with primary ion currents down to a few ten A. Even for such low projectile beam intensity, the ion induced tunneling current is clearly discernible. Other examples using a higher beam current have been presented earlier.<sup>14</sup> Normalizing the tunneling current to the projectile flux, we obtain the tunneling yield, i.e., the net number of negative elementary charges transported from the top silver to the underlying aluminum electrode per impinging projectile. It is of note that this definition does not only count hot electrons tunneling from the excited metal layer to the substrate. As shown below, there is also a contribution of hot holes being transported across the oxide barrier. The measured tunneling yield is therefore composed of two contributions arising

from excited electrons and holes, which act to (partly) counterbalance each other.

### B. Kinetic-energy dependence

The dependence of the measured tunneling yield on the kinetic impact energy of the projectile is depicted in Fig. 4. The data were obtained for singly positively charged  $\text{Ar}^+$  ions impinging under  $45^\circ$  with respect to the surface normal. Probably the most important observation is that the tunneling yield increases monotonically with impact energy, therefore clearly demonstrating that the observed tunneling current is induced by *kinetic* excitation processes. Moreover, no offset arising from the potential (ionization) energy stored in the projectile ions is visible. Note that this finding is in contrast to our earlier data<sup>14</sup> (see below). It is well known that the projectiles are neutralized in the proximity of a metal surface by either resonant electron transfer or Auger neutralization processes.<sup>27</sup> Since resonant neutralization involves mainly states located at the Fermi level, it does not lead to additional excitation of the electronic system of the solid. Instead, the resonantly neutralized projectile may de-excite, giving rise to the external emission of an electron. Auger neutralization, on the other hand, will lead to the creation of excited electrons and holes within the solid, which may in principle contribute to both external and internal emission. In fact, such “potential emission” is generally observed as a constant, impact energy independent contribution to external electron emission as soon as the excess energy  $I-\Phi$  becomes larger than the surface work function  $\Phi$  ( $I$ : ionization potential of the projectile).<sup>5</sup> Interestingly, such a contribution appears to be negligibly small in the tunneling yield. Even if the bombarding energy is reduced further (down to about 200 eV), the monotonic dependence of  $\gamma_t$  is found to continue, and the potential contribution to the measured tunneling yield can thus be estimated to be on the order of  $10^{-3}$  or below.<sup>28</sup>

The reason for the discrepancy between the data displayed in Fig. 4 and those of Ref. 14 can be explained by an experimental artifact, which was caused by the electronics measuring the tunneling current pulse and lead to an apparent offset of the tunneling yield in our earlier data. As explained above, such an offset could in principle have been expected, and therefore the problem remained unnoticed until publication of Ref. 14. In the meantime, the electronics have been carefully redesigned and the artifact has been removed. While the data measured at high impact energies are not significantly influenced, this results in a different low-energy behavior of the tunneling yield, which now clearly indicates the *absence* of such an offset (cf. Fig. 4). We are confident that this finding is correct, since it is well in accordance with the projectile charge-state dependence of the measured tunneling yield discussed below.

In principle, the observed increase in  $\gamma_t$  with increasing kinetic energy of the projectiles could be caused by two different mechanisms. First, it is clear that a faster projectile will deposit more energy into the electronic system. This can be rationalized by the fact that the electronic stopping power—which acts to slow down the projectile by inelastic interactions—increases roughly proportional to the projectile

velocity.<sup>25,29</sup> As a consequence, more excitation energy is stored in a region close to the surface. On the other hand, faster projectiles penetrate deeper into the solid, thereby exciting electrons closer to the oxide barrier. Therefore, if the transport of hot carriers through the top metal layer limits the tunneling current, the deeper penetration depth may give rise to a higher apparent yield. It is not easy to discern between these two effects. Based on our model calculations of kinetic excitation processes,<sup>30,31</sup> we believe that most of the electronic excitation giving rise to the observed tunneling current is produced in the immediate vicinity of the surface. This would render the penetration depth variation rather unimportant. Experimentally, detailed studies investigating the impact angle dependence of the measured tunneling yield are needed to clarify this point. Investigations of this kind are currently under way in our laboratory.

### C. Charge-state dependence

In order to further investigate the influence of potential energy, it is important to examine the dependence of the tunneling yield on the charge state of the projectiles. For this purpose, we compare the effect induced by  $\text{Ar}^+$  primary ions with that generated by neutral  $\text{Ar}^0$  projectiles of the same kinetic impact energy. Two experimental issues need to be discussed in respect to these measurements.

First, the pressure in the analysis chamber is different for ion or neutral bombardment due to the way the projectiles are neutralized. For the experiments with ionic projectiles the neutralizer is evacuated and the experiment is performed at the base pressure of the instrument. During measurements with neutral projectiles, on the other hand, the analysis chamber is backfilled with Argon to a pressure of up to  $10^{-6}$  mbar. Even under these conditions, however, typical mean-free paths for elastic scattering of the projectiles by residual gas atoms still exceed values on the order of 100 m, thus rendering these processes negligible. Furthermore, possible modifications of the surface work function induced by residual gas contamination do not influence our results, since the internal tunneling barrier is not affected by such changes. Note that this is in pronounced contrast to external emission measurements that are known to depend strongly on such effects.<sup>5</sup>

Second, it is necessary to measure the projectile flux onto the surface in order to determine the tunneling yield under neutral projectile bombardment. This is not a straightforward task, since the projectiles carry no charge and therefore cannot be identified by simple current measurements. They do in principle generate external electron emission as well as secondary-ion currents, but these cannot readily be employed to determine the projectile flux, since the respective yields are mostly unknown and can moreover be strongly influenced by surface contamination.

A simple strategy to determine the neutral projectile flux is to measure the remaining ion current at the surface as a function of the neutralizer gas pressure. Neglecting elastic-scattering processes within the neutralizer, the reduction in ion current can be assumed to represent the “current” of neutralized projectiles. However, besides the neglect of possible

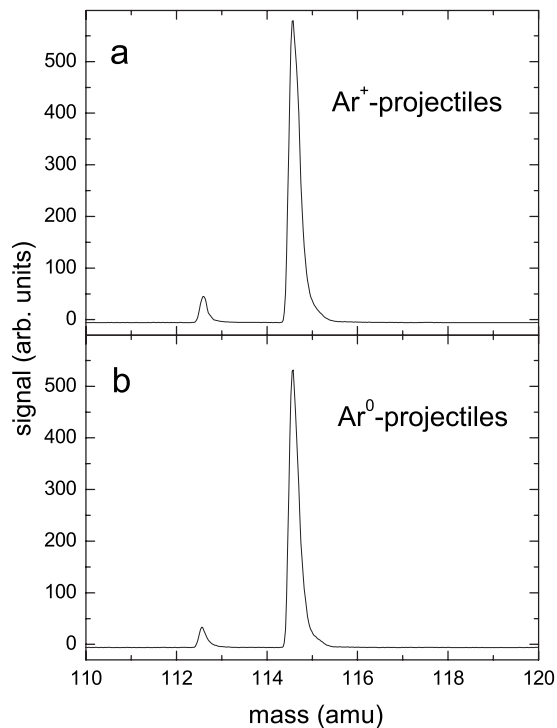


FIG. 5. Mass spectra of neutral In atoms sputtered from a clean indium surface under bombardment with 10-keV (a)  $\text{Ar}^+$  and (b)  $\text{Ar}^0$  projectiles.

beam shape variations due to scattering processes, this strategy relies on the assumption that electron emission and secondary ion yields at the bombarded surface are unaffected by the projectile charge state. This assumption, however, appears highly uncertain.<sup>32,33</sup>

A better way to solve the problem is to utilize the emission of sputtered neutral particles from the bombarded target surface. It is well known that—at least for metallic solids—the sputtering yield, i.e., the average number of atoms released from the surface due to one single projectile impact, is independent of the projectile charge.<sup>19,34</sup> Therefore, measuring the flux of sputtered atoms allows to determine the projectile flux regardless of their charge state. Moreover, it is known that the large majority of atoms sputtered from a clean metal surface are emitted in the neutral state.<sup>33,35,36</sup> In order to obtain information representative of the sputtered flux, it is therefore mandatory to detect the *neutral* atoms leaving the surface. These particles need to be postionized prior to mass spectrometric detection, which is accomplished here by means of single-photon ionization in an intense pulsed UV laser beam. Measuring the mass spectrometric signal of postionized neutral atoms sputtered from a reasonably clean metal target surface then provides an elegant solution to the problem of projectile flux determination.

Mass spectra of sputtered neutral atoms emitted from a clean indium surface under bombardment with  $\text{Ar}^+$  and  $\text{Ar}^0$  projectiles are shown in Fig. 5. The spectrum shown in panel (a) was recorded without backfilling the neutralizer. Blanking the ion beam by means of deflection plates produces a negligible background of less than 0.2% of the displayed signal, and therefore the entire signal is induced by  $\text{Ar}^+$  pro-

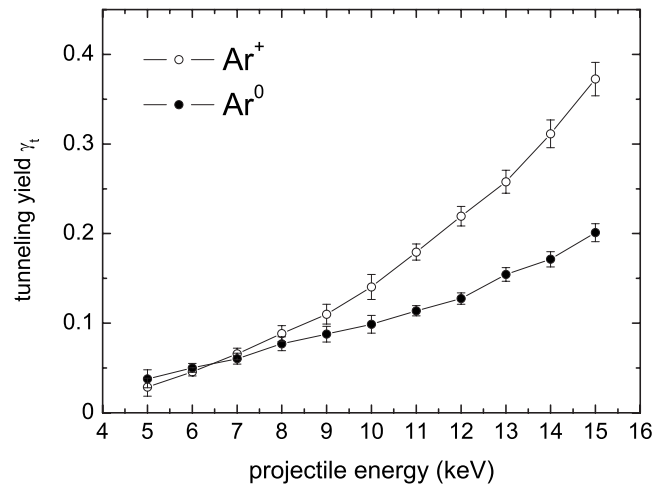


FIG. 6. Tunneling yield vs kinetic impact energy of charged and neutral Ar projectiles impinging onto the silver surface of a MIM junction.

jectiles. Filling the neutralizer with argon and blanking the ion beam produces the spectrum shown in panel (b), which must therefore be entirely produced by neutral projectiles. The fact that the signal is lower by about 10% than in panel (a) is caused by elastic scattering of the projectile beam within the neutralizing gas cell.

Taking the SNMS signal depicted in Fig. 5 as a reference of the projectile flux, it is now possible to determine the tunneling yield also for neutral projectiles. The results are shown in Fig. 6. It is immediately evident that the influence of the projectile charge state does not simply manifest as an offset to the impact energy dependence curve. At high impact energies, a smaller tunneling yield is observed under bombardment with neutral projectiles, the difference increasing with increasing energy. A similar effect has been observed for external electron emission from gold<sup>32</sup> and molybdenum<sup>37</sup> surfaces bombarded by  $\text{Ar}^+$  and  $\text{Ar}^0$  projectiles. As pointed out in Ref. 32, this effect cannot be produced by potential emission, since the respective yield contribution would be independent of or even decrease with increasing impact energy. Instead, it was attributed to a change of the kinetic emission process, generated by a charge-state dependence of the electronic stopping power experienced by the projectile. At sufficiently large impact energy, the projectile ion does not spend enough time in close proximity to the surface to be fully neutralized before its actual impact. Therefore, it will with a certain probability retain its original charge state until it penetrates the surface. Once inside the crystal, the projectile will undergo fast electron capture and loss and rapidly assume an equilibrium charge state (close to neutral) within about a nanometer of travel.<sup>32</sup> Since the unscreened Coulomb potential leads to a larger scattering cross section, energy transfer to free conduction-band electrons is more efficient in the ionic state, thus leading to a larger electronic stopping power. In fact, Lakits *et al.*<sup>32</sup> calculated roughly a factor of 4 between the stopping power of slow  $\text{H}^+$  and  $\text{H}^0$  penetrating a metal of  $r_s \sim 3$  (the appropriate value for Ag). As a consequence, a charged projectile will on average deposit more energy into

the electronic system, leading to a larger tunneling yield. With increasing impact energy, the dwell time for neutralization in front of the surface decreases, therefore increasing the survival probability of the initial projectile charge state. At 15 keV,  $\text{Ar}^+$  therefore induces almost twice the tunneling current as an  $\text{Ar}^0$  projectile. For energies below approximately 5 keV, on the other hand, both yields appear to be practically identical within the experimental error, indicating complete projectile neutralization before the actual impact. Assuming the interaction range above the surface to have an extension of about 1 Å, this converts to a neutralization time of about 1 fs which seems reasonable.<sup>27</sup>

#### D. Film thickness dependence

In principle, kinetic excitation processes induced by a projectile impact are not restricted to the very surface of the bombarded sample. Depending on their penetration range, projectiles can deposit energy at various depths below the surface, thus leading to an initial depth distribution of hot carriers (electrons and holes) as well as recoil atoms which can then again produce further kinetic excitation. In a MIM device, on the other hand, hot carriers are detected at the metal-oxide interface. As outlined above, the thickness of the top metal film was chosen as such to completely enclose the impact induced particle kinetics, thus preventing hot carrier generation directly at the buried insulating layer. As a consequence, the excited carriers must travel to the oxide-metal interface, and the measured signal will therefore depend on the thickness of the top metal film. This dependence was investigated in two ways.

First, the sample was subjected to the (pulsed) ion beam for a prolonged time. As the ion fluence accumulates, the surface is then gradually eroded due to sputtering, thus *reducing* the top metal film thickness within the bombarded area. Since the sputter yield—i.e., the average number of sputtered atoms per projectile ion impact—of silver under  $\text{Ar}^+$  ion bombardment is known, the accumulated ion fluence can be converted into eroded depth, and the tunneling yield can be measured as a function of the remaining film thickness. An example of such an experiment is shown in Fig. 7. The data were acquired with 10-keV  $\text{Ar}^+$  projectiles impinging under  $45^\circ$  with respect to the surface normal. Averaging documented experimental sputter yield data—measured under normal incidence—over the available literature, one obtains a yield of about ten removed atoms per projectile ion.<sup>38</sup> In order to estimate the influence of the impact angle, we utilize computer simulations using the SRIM2006 program package. The resulting yield for (polycrystalline or amorphous) silver is  $Y=12.5$  atoms/ion for  $45^\circ$  incidence. The eroded depth is then calculated as

$$z = \frac{Yf}{n}, \quad (3)$$

where  $f$  is the accumulated ion fluence and  $n$  is the atom density of the sample ( $58.5 \text{ nm}^{-3}$  for silver).

Two observations are immediately evident in Fig. 7. First, it is seen that the MIM device remained intact down to a top metal film thickness of about 6 nm. Note that this thickness

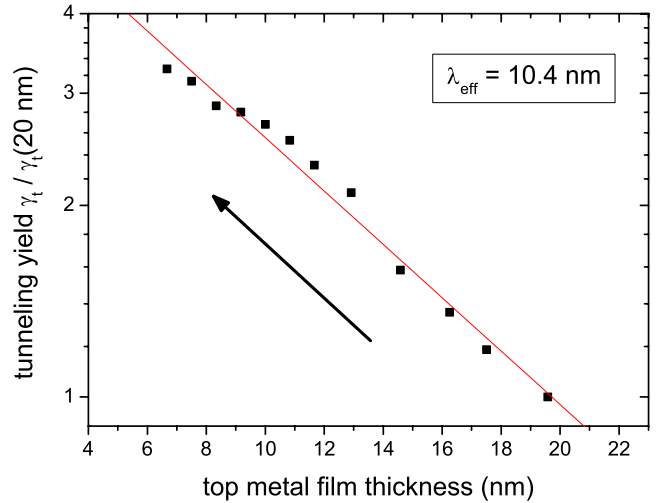


FIG. 7. (Color online) Dependence of tunneling yield on the remaining film thickness during sputter erosion of the top metal layer of a MIM structure. The black arrow indicates the direction of the measurement. The data were obtained using an  $\text{Ag}|\text{AlOx}|\text{Al}$  MIM structure bombarded with 10-keV  $\text{Ar}^+$  ions and normalized to the yield measured at the initial film thickness of 20 nm.

corresponds almost exactly to the calculated mean range of the projectiles (6.3 nm) under the employed bombarding conditions. Hence, if the remaining film thickness becomes smaller than this value, projectiles start penetrating the metal-oxide interface, thereby creating enough damage to the oxide layer for the tunnel junction to break down. The second important observation in Fig. 7 is that the tunneling yield increases with decreasing top metal film thickness. This finding is qualitatively expected, since hot carriers generated in the proximity of the surface need to travel shorter distances to the buried tunnel junction, thereby losing less energy due to electron-electron scattering and enhancing the probability of overcoming the tunneling barrier. Fitting an exponential slope to the data in the thickness range above 10 nm, we obtain an effective attenuation length of about 10...11 nm. In principle, this quantity provides information about the average ballistic mean-free path of the excited charge carriers in the top metal film. It should be noted, however, that the mean-free path will strongly depend on the excitation energy and, in addition, may not necessarily be the same for electrons and holes.

An alternative way to approach the problem is to *increase* the top metal film thickness by depositing additional material on the surface. In this experiment, the MIM junction was repeatedly transferred to a connected vacuum chamber, cooled down to 130 K, and then coated with a few nm of additional silver. The amount of deposited material and, hence, the increment in film thickness was measured with a calibrated quartz crystal microbalance. Then, the device was allowed to warm up to room temperature and transferred back to the analysis chamber, where the resulting tunneling yield was determined. The result of such an experiment is displayed in Fig. 8. As expected, the measured tunneling yield decreases with increasing top metal film thickness. A very similar thickness dependence has been observed if the hot carriers are excited by photon irradiation instead of fast

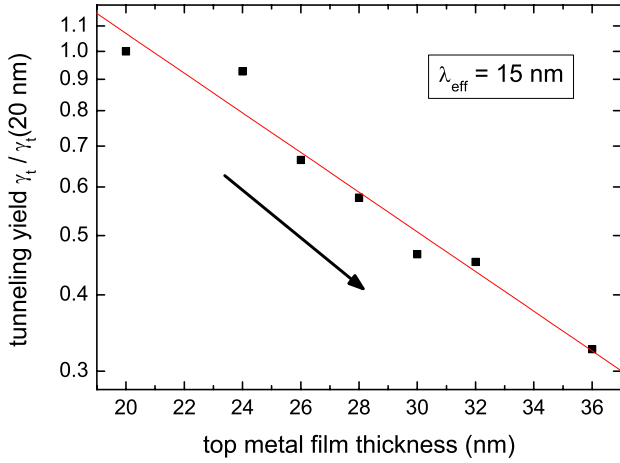


FIG. 8. (Color online) Top metal film thickness dependence of the tunneling yield for sequential vapor deposition of additional surface layers. The measuring sequence is indicated by the black arrow. The data were obtained using an Ag|AlOx|Al MIM structure bombarded with 10-keV Ar<sup>+</sup> ions and normalized to the yield measured at the initial film thickness of 20 nm.

projectile impact.<sup>39</sup> Fitting an exponential decay to this data set, we obtain an effective mean-free path of 15 nm, which is of the same order but slightly larger than the value obtained via sputter erosion. The difference between both values is most likely related to the fact that different MIM devices were used in both experiments. Moreover, it is clear that prolonged ion bombardment produces defects in the top metal film, which then may act to decrease the electron mean-free path. In contrast, deposition (and annealing) of more silver at the surface leads to growth of a more ideal material, which then exhibits a longer average mean-free path of the excited hot carriers.

**E. Bias voltage dependence**

All experiments described so far have been performed without a potential difference between the two metal electrodes of the MIM device. In this section, we investigate the influence of a bias voltage applied between these electrodes on the measured tunneling yields. The main goal behind such an experiment is to obtain information about the spectrum of excitations generated by the particle kinetics. In order to visualize this idea, Fig. 9 depicts the (one-dimensional) energy diagram representing the tunnel junction. The band structure has been simplified such that the two metal electrodes are approximated as free-electron gases, whereas the oxide is described by the bottom of the conduction band and top of its valence band. Both levels are separated by the band gap and vary in energy across the oxide film, since the tunneling barrier (i.e., the difference between the Fermi level and the bottom of the oxide conduction band) depends on the metal. From an analysis of the *I-V* characteristic measured at low temperature,<sup>15</sup> the respective barrier heights have been determined as  $\Phi^{Ag}=3.9$  eV and  $\Phi^{Al}=2.4$  eV at the Ag-AlOx and the Al-AlOx interface, respectively. To first order, the potential barrier determining the tunneling current is therefore trapezoidally shaped as indicated in the left panel of Fig. 9. The band gap of the oxide layer is determined as  $E_{gap}=6.7$  eV from the onset of optical absorption measured in thin amorphous, anodized AlO<sub>x</sub> films.<sup>40</sup> Note that this value is significantly smaller than that of bulk, single crystalline Al<sub>2</sub>O<sub>3</sub>. As will be shown below, this difference is essential in order to understand the measured bias voltage dependence.

Without any bias voltage applied, the Fermi levels of both metal electrodes are virtually the same (apart from a small thermoelectric potential difference in the microvolt range), and no net current is flowing without the ion beam impinging onto the top metal (silver) surface. Once the surface is exposed to the ion beam, hot electrons are generated in the top

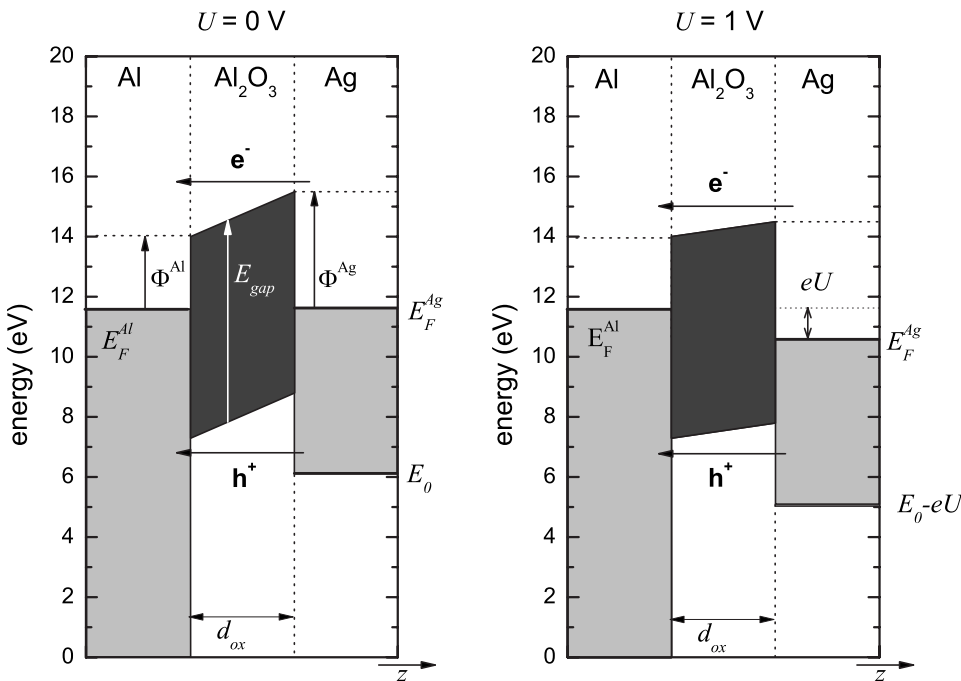


FIG. 9. Energy diagram of a MIM tunnel junction without (left panel) and with (right panel) a bias voltage applied between the two metal electrodes. The tunnel current of hot electrons and holes kinetically excited in the top silver layer is displayed as arrows from right to left above and below the barrier, respectively.

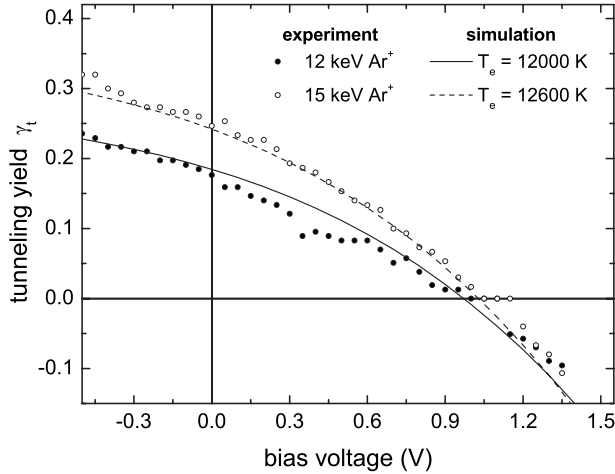


FIG. 10. Tunneling yield vs bias voltage applied between both metal electrodes of a MIM device for two different kinetic energies of the  $\text{Ar}^+$  ions impinging onto the top metal surface. Lines: simulated spectrum calculated as described in Sec. III F using  $\Phi^{\text{Ag}} = 3.9$  eV,  $\Phi^{\text{Al}} = 2.4$  eV,  $E_{\text{gap}} = 6.7$  eV,  $d_{\text{ox}} = 2.5$  nm,  $E_F^{\text{Al}} = 11.6$  eV and  $E_F^{\text{Ag}} = 5.5$  eV,  $\delta A_{\text{casc}} = 1$  nm<sup>2</sup>,  $\delta t = 6.2$  fs and the indicated values of the electron temperature.

metal electrode, which may then tunnel through the barrier into the underlying substrate electrode. Applying a bias voltage  $U$  as indicated in Fig. 9, hot electrons with excitation energies below  $e \cdot U$  are effectively blocked from tunneling. Variation of the bias voltage therefore in principle allows to obtain information about the excitation spectrum of the generated hot charge carriers.

The result of such an experiment is displayed in Fig. 10. Note that the dc tunneling current produced by any nonzero bias voltage has been subtracted, and the displayed data therefore solely represent the (additional) tunneling yield induced by the primary ion impact. The polarity of the bias voltage is chosen such that positive values correspond to the situation depicted in the right panel of Fig. 9, where the Fermi level of the silver top metal electrode is lowered with respect to that of the aluminum substrate. It is seen that this reduces the tunneling yield as expected, while a negative

voltage enhances the yield. A striking observation in Fig. 10 is the fact that the ion induced tunnel current goes through zero at  $U \sim 1$  V and reverses its sign if the bias voltage is increased further. This behavior is completely different from that of the dc background tunnel current (see Fig. 3) and cannot be explained in terms of kinetic hot electron generation alone.

In order to understand the sign reversal, we have to include holes into the picture. As indicated in Fig. 9, hot holes generated in the top metal conduction band at energies below the Fermi level can in principle tunnel via the oxide valence band. Such two-band tunneling processes are well known and have been described theoretically.<sup>41</sup> In effect, the energy difference between the Fermi level and the top of the oxide valence band acts as a tunneling barrier for the holes. Details regarding the modeling of this process have been published elsewhere<sup>39</sup> and are given below. Kinetically excited holes will therefore also lead to a tunneling current, which is of opposite sign and acts to counterbalance the electron current. Application of a bias voltage now alters the shape of the potential barriers experienced by hot electrons and holes as indicated in the right panel of Fig. 9. As a consequence, the balance between electron and hole tunneling currents is shifted in favor of the holes, thereby reducing the net current flowing across the oxide layer. It is obvious that this effect may lead to a complete extinction or even sign reversal of the measured net-tunneling current.

### F. Tunneling model

In order to interpret the data presented in Fig. 10, it is necessary to model the measured tunneling current using the concepts outlined in Sec. III E. The trapezoidal potential barrier is parametrized as

$$V(U, z) = E_F^{\text{Al}} + \Phi^{\text{Al}} + \frac{(\Phi^{\text{Ag}} - \Phi^{\text{Al}} - U)}{d_{\text{ox}}}. \quad (4)$$

Based on the treatment of Franz<sup>42</sup> and Kane,<sup>43</sup> the two-band tunneling probability via either the oxide conduction or valence band is described as<sup>41</sup>

$$p(E, U) = \exp \left[ -2 \sqrt{\frac{2m}{\hbar^2}} \int_0^{d_{\text{ox}}} \left\{ \frac{[E - V(U, z)][E - V(U, z) + E_{\text{gap}}] - E_p}{E_{\text{gap}}} \right\} dz \right], \quad (5)$$

where  $m$  and  $E$  denote the effective mass (which, for simplicity, is taken as the free-electron mass here) and energy of the electrons and  $d_{\text{ox}}$  is the oxide layer thickness.

In order to describe the kinetic tunneling yield, we assume the electron temperature  $T_e$  of the electron gas representing the top metal layer to be elevated for a short time  $\delta t$  during the collision cascade initiated by a projectile ion impact. Since the mean range of the projectiles is small compared to

the top metal film thickness, we assume the second electron gas representing the aluminum substrate to remain unexcited (at room temperature) and calculate the resulting tunneling current density across the oxide layer as a function of  $T_e$ . This value is then multiplied by  $\delta t$  and the lateral surface area  $\delta A_{\text{casc}}$  affected by the collision cascade in order to determine the net charge transported through the tunnel junction per projectile impact. Dividing this quantity by the el-

elementary charge then results in the predicted tunneling yield.

The tunneling current density between two electron gases at temperatures  $T^{\text{Ag}}=T_e$  and  $T^{\text{Al}}=T_0$  is given by<sup>39</sup>

$$j_t(U, T_0, T_e) = \frac{4\pi em}{h^3} \int_{E_0(U)}^{\infty} dE_z \int_0^{\infty} dE_p \{ p(E_z, E_p, U) \cdot [f_{\text{Ag}}(E_z + E_p, T_e, U) - f_{\text{Al}}(E_z + E_p, T_0)] \}, \quad (6)$$

where  $e$  is the elementary charge,  $E_z = \hbar^2 k_z^2 / 2m$  and  $E_p = \hbar^2 k_p^2 / 2m$  denote the energies associated with the electron velocity components perpendicular ( $v_z$ ) and parallel to the junction and  $E = E_z + E_p$ . All energies are counted from the bottom of the Al conduction band. The lower limit  $E_0(U) = \max(0, E_F^{\text{Al}} - E_F^{\text{Ag}} - eU)$  in the first integral of Eq. (6) ensures that no integration is performed over energies below the conduction band of the silver or aluminum electrode, where no electronic states exist. The quantities  $f_{\text{Ag}}$  and  $f_{\text{Al}}$  denote the Fermi distribution in both metals given by

$$f_{\text{Al}}(E, T_0) = \left[ \exp\left(\frac{E - E_F^{\text{Al}}}{k_B T_0}\right) + 1 \right]^{-1} \quad \text{and}$$

$$f_{\text{Ag}}(E, T_e, U) = \left[ \exp\left(\frac{E - E_F^{\text{Al}} + eU}{k_B T_e}\right) + 1 \right]^{-1}.$$

In order to apply the model to simulate the measured tunneling yield spectra, we use the fixed MIM device parameters  $\Phi^{\text{Ag}}=3.9$  eV,<sup>15</sup>  $\Phi^{\text{Al}}=2.4$  eV,<sup>15</sup>  $E_{\text{gap}}=6.7$  eV,<sup>40</sup> and  $d_{\text{ox}}=2.5$  nm. The Fermi energies of  $E_F^{\text{Al}}=11.6$  eV and  $E_F^{\text{Ag}}=5.5$  eV are taken from the literature.<sup>44</sup> Since  $\delta \cdot \delta A_{\text{casc}}$  constitutes a constant normalization factor, the only free parameter determining the calculated bias voltage dependence is the electron temperature  $T_e$ . The resulting spectra are displayed in Fig. 11. In order to allow a better comparison, the curves calculated by Eq. (6) for different values of  $T_e$  have been normalized to the respective value at zero-bias voltage. The first important observation is that the experimentally measured sign reversal of the tunneling current can be qualitatively reproduced by the model calculation. Moreover, it is evident that—for a given set of MIM device parameters—the electron temperature is strongly correlated with the bias voltage at which the tunneling yield crosses zero. As a consequence of this behavior, we can determine  $T_e \sim 12000$  K and  $\sim 12600$  K from the measured crossing points (Fig. 10) at  $\text{Ar}^+$  ion energies of 12 and 15 keV, respectively. At first sight, these temperatures appear very large. This point will be further discussed below. The finding that larger kinetic impact energy leads to a higher excitation “temperature,” on the other hand, appears sensible.

To understand the physics behind the simulated spectra, it is of interest to look at the contribution of charge carriers at different excitation energies to the total tunneling yield. We visualize this by plotting the integrand of the first integral in Eq. (6) as a function of  $E_z$  in Fig. 12. Note that the abscissa ( $E_z$ ) is plotted vertically in Fig. 12, and (positive) current contributions to the right-hand side correspond to electrons,

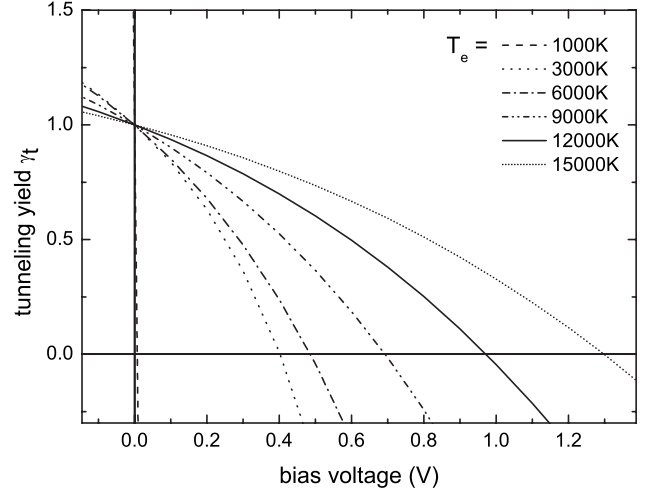


FIG. 11. Calculated bias voltage dependence of the MIM tunneling yield as a function of the electron temperature in the top silver metal electrode. The data were calculated by Eq. (6) using  $\Phi^{\text{Ag}}=3.9$  eV,  $\Phi^{\text{Al}}=2.4$  eV,  $E_{\text{gap}}=6.7$  eV,  $d_{\text{ox}}=2.5$  nm,  $E_F^{\text{Al}}=11.6$  eV and  $E_F^{\text{Ag}}=5.5$  eV and normalized to the value at zero-bias voltage.

while (negative) contributions to the left-hand side arise from holes being transported from the top metal to the substrate.

From Fig. 12, it is obvious that the nature of the current flowing across the oxide layer depends on the electron temperature. In the region of “low” temperatures at or below  $\sim 1000$  K, one observes a typical tunneling current with major contributions arising from energies around the Fermi level. At zero-bias voltage, the contributions of electrons and holes are approximately equal, resulting in a relatively small net positive tunneling current. Applying a (positive) bias voltage modifies the shape of the potential barrier as indicated on the right-hand side of the figure, thereby shifting the weight toward the holes. As a consequence, the (negative) contribution of holes overcompensates that of the electrons and the tunneling current has shifted its sign, with the largest current contribution arising at the Al substrate Fermi level.

The situation completely changes if the temperature exceeds values of several thousand kelvin. Now, the major contribution to the observed current of electrons and holes arises from energies located at the top of the respective potential barrier. In this case, the “true” tunneling process at the Fermi level is apparently negligible, and the observed current mainly represents an “over-the-barrier” conduction mechanism. Due to the larger height of the potential barrier for holes (4.3 eV) as compared to that for electrons (3.9 eV), the electron contribution outbalances that of the holes at zero-bias voltage, thus leading to a positive net “tunneling” current. Application of a positive bias voltage again increases the weight of holes, leading to the observed zero crossing of the net current at a temperature dependent value of  $U$ . This is nicely visible at  $T_e=3000$  K and  $U=0.5$  V, where the contributions of both carrier types just counterbalance each other. The pronounced asymmetry of the electron and hole peaks observed at  $T_e=12000$  K and  $U=1$  V arises from the fact that the maximum possible excitation energy of holes is

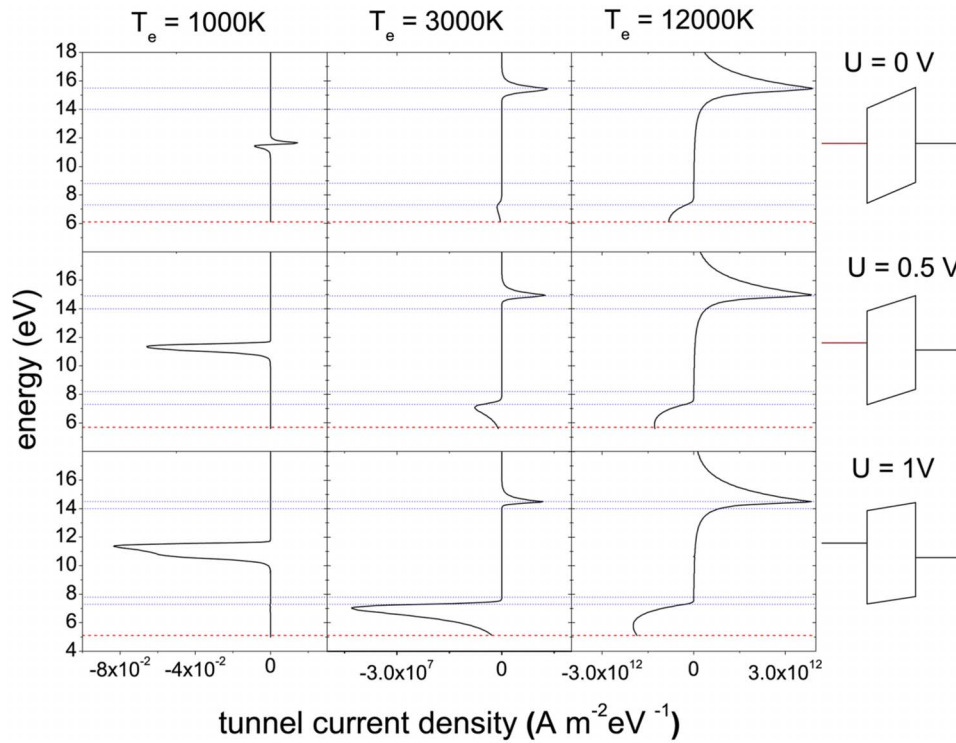


FIG. 12. (Color online) Contribution of different excitation energies  $E_z$  to the simulated tunneling current calculated by Eq. (6) for three different electron temperatures and three different bias voltages. Positive values of the tunneling current density correspond to contributions of electrons, whereas negative values denote the contribution of holes. The (blue) dotted lines represent the height of the tunneling barrier at the AllAlOx (left) and AlOx|Ag (right) interfaces; the (red) dashed line denotes the bottom of the Ag conduction band.

restricted to the Fermi energy of silver, while the excitation energy of electrons is in principle unrestricted.

Besides the sign reversal, a second important piece of information is the measured magnitude of the tunneling yield. Since Eq. (6) predicts absolute values of the tunneling current density, we can calculate the yield by assuming values of  $\delta t$  and  $\delta A_{\text{casc}}$ . Based on our theoretical model calculations of kinetic excitation processes<sup>31</sup> (see below), we fix the lateral extension of the impact induced local hot spot to  $\delta A_{\text{casc}} \sim 1 \text{ nm}^2$ . Although there is some ambiguity regarding this value, its order of magnitude is certainly correct. With  $T_e$  and  $\delta A_{\text{casc}}$  being fixed, we can use the measured tunneling yield to determine the lifetime of the hot spot. As a result, we obtain  $\delta t \sim 6 \text{ fs}$ . The tunneling yield calculated with these values is depicted in Fig. 10. Note that the two lines represent data which were obtained by calculating the absolute value of the tunneling current density and multiplying with  $\delta t \cdot \delta A_{\text{casc}}$ , using the same set of parameters except for the two different electron temperatures indicated in the figure. At zero-bias voltage, the displayed data correspond to calculated current densities of  $5.2 \times 10^{16}$  and  $6.5 \times 10^{16} \text{ nA/mm}^2$ , respectively, which are by many orders of magnitude larger than the dc tunneling current displayed in Fig. 3. It is seen that both experimental data sets measured at two different kinetic impact energies can be well reproduced by the model calculation. This finding is important since the absolute magnitude of the predicted yield depends very sensitively on the assumed electron temperature.

At first sight, the value of  $\delta t$  deduced from the above analysis appears surprisingly small compared to the typical temporal duration (picoseconds) of an atomic collision cascade. To investigate this apparent discrepancy, we revert to our model calculations of the kinetic excitation process which have been described in great detail elsewhere.<sup>30,31,45–48</sup>

Briefly, the particle dynamics induced by the projectile impact are followed by a classical molecular dynamics computer simulation, while the electronic system of the bombarded solid is approximated as a free-electron gas. The transfer from kinetic to electronic excitation energy is treated by means of two independent mechanisms, namely (i) electronic friction experienced by all moving particles and (ii) electron promotion in close binary collisions. The potential energy of the projectile ions is neglected in these calculations. Transport of the resulting electronic excitation energy is described in terms of a diffusive approach employing a space and time dependent diffusivity of electronic heat.

As a result of such a calculation, Fig. 13 shows the temporal variation of the electron temperature at the surface of

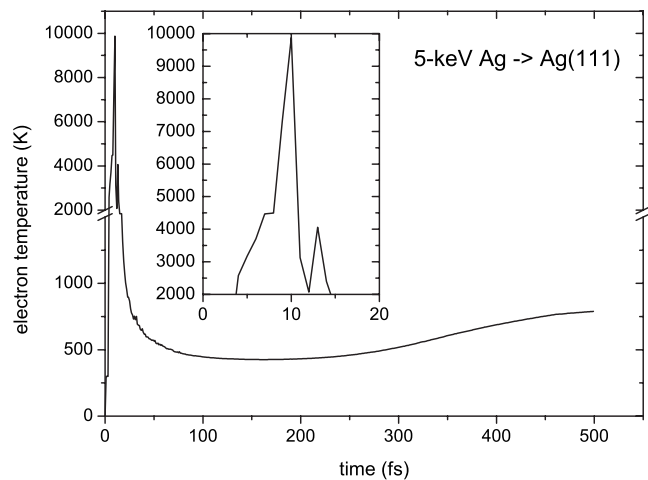


FIG. 13. Calculated electron temperature at the (111) surface of a silver single crystal vs time after the impact of a 5-keV Ag atom. The data were averaged over 120 individual impact events.

an Ag(111) crystal generated by the impact of a 5-keV Ag atom. The data were averaged over 120 individual impact events; details of the calculation will be published elsewhere.<sup>49</sup> It is seen that shortly ( $\sim 10$  fs) after the projectile impact a hot spot forms at the surface, the duration of which is restricted to only a few femtoseconds. During this time interval, temperatures on the order of  $10^4$  K can be reached, which then rapidly decrease again due to the fast conduction of electronic heat away from the impact zone.

Both findings are in good agreement with the values of  $T_e$  and  $\delta t$  derived from the analysis of the experimental MIM tunneling yields. In fact, the almost quantitative agreement appears to be rather fortuitous in view of the different projectile species and energies employed in the experiments and calculations. Moreover, one should not forget that the two-temperature model parametrizes the electron energy distribution at the tunnel junction, whereas the data displayed in Fig. 13 refer to a local hot spot created at the surface. At present, it is not clear how transport of excited carriers across the top metal layer may influence their energy distribution. Experimentally, this question might be tackled by measuring the bias voltage dependence for varying film thickness and projectile impact angle, while a theoretical description requires to explicitly model the electron-electron interaction. Studies in these directions are currently under way in our laboratory. Nevertheless, the data in Fig. 10 reveal that the simple two-temperature tunneling model employed here is still useful to derive valuable information about the excitation spectrum generated by the kinetic excitation process of solids.

#### IV. CONCLUSIONS

The experiment reported here demonstrates that MIM tunnel junctions can be successfully employed to investigate the kinetic excitation of solids induced by energetic particle bombardment. It is shown that ion irradiation of the top metal surface of a MIM device results in a measurable tunneling current into the underlying substrate electrode, which

is generated by hot excited charge carriers generated by the projectile impact. The measured tunneling yield strongly depends on the projectile energy, thus clearly demonstrating the kinetic nature of the excitation process. While we observe only a negligible yield offset induced by the potential (ionization) energy of the  $\text{Ar}^+$  projectile ions, there are still distinct differences between ionic and neutral projectiles, which are attributed to a charge-state dependence of the electronic stopping power experienced by the projectile after penetrating the surface. The observed difference becomes smaller with decreasing impact energy, since neutralization of the projectile ions before actually reaching the surface becomes more and more efficient with increasing residence time in close proximity outside the solid. The observed tunneling yield is found to depend on the thickness of the top metal film in a way consistent with an effective mean-free path of the excited charge carriers on the order of 10...15 nm.

Application of a bias voltage between the two electrodes of the tunnel junction allows to gain information about the excitation energy spectrum of the generated charge carriers. The data clearly show that a meaningful interpretation of the observed bias voltage dependence is only possible if both excited electrons *and* conduction-band vacancies (holes) are included in the analysis. It is shown that the measured data are consistent with a simple two-temperature tunneling model assuming the formation of a transient local hot spot generated by the projectile impact. The analysis suggests that the measured tunneling current arises from a very fast, short-lived local electronic heating of the irradiated surface, which is induced by the electronic energy loss of the impinging projectile while penetrating the surface.

#### ACKNOWLEDGMENTS

We are greatly indebted to the Deutsche Forschungsgemeinschaft for financial support in the frame of the Sonderforschungsbereich 616 entitled "Energy Dissipation at Surfaces." We also thank D. Kovacs for many valuable discussions.

\*Corresponding author; andreas.wucher@uni-due.de

<sup>1</sup>J. F. Ziegler, *Appl. Phys. Lett.* **31**, 544 (1977).

<sup>2</sup>P. Sigmund, in *Sputtering by Particle Bombardment I*, edited by R. Behrisch (Springer, Berlin, 1981), Vol. 1, p. 9.

<sup>3</sup>*Sputtering by Particle Bombardment*, edited by R. Behrisch *et al.* (Springer, New York, 1981), Vol. I; *Sputtering by Particle Bombardment*, edited by R. Behrisch *et al.* (Springer, Berlin, 1983), Vol. II; *Sputtering by Particle Bombardment*, edited by R. Behrisch and K. Wittmaack (Springer, Berlin, 1991), Vol. III; *Sputtering by Particle Bombardment*, edited by R. Behrisch and W. Eckstein (Springer, Berlin, 2007), Vol. IV.

<sup>4</sup>Although the term "hole" might not be semantically correct to describe a conduction-band vacancy, we use it here for simplicity and consistency with our previous publications.

<sup>5</sup>R. A. Baragiola, *Nucl. Instrum. Methods Phys. Res. B* **78**, 223 (1993).

<sup>6</sup>W. O. Hofer, *Scanning Microsc.* **4**, 265 (1990).

<sup>7</sup>R. A. Baragiola, in *Low Energy Ion-Surface Interactions*, edited by J. W. Rabalais (Wiley, Chichester, 1994), p. 187.

<sup>8</sup>M. Roesler, W. Brauer, J. DeVooght, J. C. Dehaes, A. Dubus, M. Cailler, and J.-P. Ganachaud, *Particle Induced Electron Emission I* (Springer, New York, 1991).

<sup>9</sup>J. Schou, *Phys. Rev. B* **22**, 2141 (1980).

<sup>10</sup>J. Lindhard, M. Scharff, and H. E. Schiøtt, *Mat. Fys. Medd. K. Dan. Vidensk. Selsk.* **33**, 1 (1963).

<sup>11</sup>G. Falcone and Z. Sroubek, *Radiat. Eff. Defects Solids* **109**, 253 (1989).

<sup>12</sup>G. Falcone and Z. Sroubek, *Phys. Rev. B* **39**, 1999 (1989).

<sup>13</sup>G. Falcone and Z. Sroubek, *Phys. Rev. B* **38**, 4989 (1988).

<sup>14</sup>S. Meyer, D. Diesing, and A. Wucher, *Phys. Rev. Lett.* **93**, 137601 (2004).

<sup>15</sup>D. Diesing, G. Kritzer, M. Stermann, D. Nolting, and A. Otto, *J.*

- Solid State Electrochem. **7**, 389 (2003).
- <sup>16</sup>D. Diesing, G. Kritzler, and A. Otto, in *Solid-Liquid-Interfaces: Macroscopic Phenomena—Microscopic Understanding*, edited by K. Wandelt and S. Thurgate (Springer, Berlin, 2003), p. 365.
- <sup>17</sup>D. Diesing, S. Russe, A. Otto, and M. M. Lohrengel, Ber. Bunsenges. Phys. Chem. **99**, 1402 (1995).
- <sup>18</sup>S. Meyer, D. Diesing, and A. Wucher, Nucl. Instrum. Methods Phys. Res. B **230**, 608 (2005).
- <sup>19</sup>F. Aumayr and H. Winter, Philos. Trans. R. Soc. London **362**, 77 (2004).
- <sup>20</sup>M. Wahl and A. Wucher, Nucl. Instrum. Methods Phys. Res. B **94**, 36 (1994).
- <sup>21</sup>C. Staudt and A. Wucher, Phys. Rev. B **66**, 075419 (2002).
- <sup>22</sup>Ch. Heuser, S. Meyer, and A. Wucher (unpublished).
- <sup>23</sup>D. Diesing, A. W. Hassel, and M. M. Lohrengel, Thin Solid Films **342**, 282 (1999).
- <sup>24</sup>Information about the program package SRIM 2006 can be found at <http://www.srim.org>
- <sup>25</sup>J. F. Ziegler, J. Biersack, and M. D. Ziegler, *The Stopping and Range of Ions in Matter* (SRIM, Chester, 2008).
- <sup>26</sup>E. Z. Luo, S. Heun, M. Kennedy, J. Wollschlager, and M. Henzler, Phys. Rev. B **49**, 4858 (1994).
- <sup>27</sup>H. D. Hagstrum, in *Chemistry and Physics of Solid Surfaces VII*, edited by R. Vanselow and R. F. Howe (Springer, Berlin, 1988), p. 341.
- <sup>28</sup>D. Kovacs, D. Diesing, and A. Wucher (unpublished).
- <sup>29</sup>J. Lindhard and M. Scharff, Phys. Rev. **124**, 128 (1961).
- <sup>30</sup>A. Duvenbeck, Z. Sroubek, and A. Wucher, Nucl. Instrum. Methods Phys. Res. B **228**, 325 (2005).
- <sup>31</sup>A. Duvenbeck and A. Wucher, Phys. Rev. B **72**, 165408 (2005).
- <sup>32</sup>G. Lakits, A. Arnau, and H. Winter, Phys. Rev. B **42**, 15 (1990).
- <sup>33</sup>M. L. Yu, in *Sputtering by Particle Bombardment III*, edited by R. Behrisch and K. Wittmaack (Springer, Berlin, 1991), Vol. III, p. 91.
- <sup>34</sup>G. Hayderer, S. Cernusca, V. Hoffmann, D. Niemann, N. Stolterfoht, M. Schmid, P. Varga, H. P. Winter, and F. Aumayr, Nucl. Instrum. Methods Phys. Res. B **182**, 143 (2001).
- <sup>35</sup>A. Benninghoven, F. G. Rüdener, and H. W. Werner, *Secondary Ion Mass Spectrometry: Basic Concepts, Instrumental Aspects and Trends* (Wiley, New York, 1987).
- <sup>36</sup>K. Wittmaack, in *Inelastic Ion-Surface Collisions*, edited by N. H. Tolk, J. C. Tully, W. Heiland, and C. W. White (Academic, New York, 1977), p. 153.
- <sup>37</sup>D. B. Medved, P. Mahadevan, and J. K. Layton, Phys. Rev. **129**, 2086 (1963).
- <sup>38</sup>H. H. Andersen and H. L. Bay, in *Sputtering by Particle Bombardment I*, edited by R. Behrisch (Springer, Berlin, 1981), Vol. 1, p. 145.
- <sup>39</sup>D. A. Kovacs, J. Winter, S. Meyer, A. Wucher, and D. Diesing, Phys. Rev. B **76**, 235408 (2007).
- <sup>40</sup>E. T. Arakawa and M. W. Williams, J. Phys. Chem. Solids **29**, 735 (1968).
- <sup>41</sup>K. H. Gundlach, J. Appl. Phys. **44**, 5005 (1973).
- <sup>42</sup>W. Franz, in *Handbuch der Physik*, edited by S. Flügge (Springer, Berlin, 1956), Vol. 17, p. 155.
- <sup>43</sup>E. O. Kane and E. I. Blount, in *Tunneling Phenomena in Solids*, edited by E. Burnstein and S. Lundquist (Plenum, New York, 1963), p. 79.
- <sup>44</sup>C. Kittel, *Introduction to Solid State Physics* (Wiley, New York, 1971), p. 249.
- <sup>45</sup>A. Duvenbeck, F. Sroubek, Z. Sroubek, and A. Wucher, Nucl. Instrum. Methods Phys. Res. B **225**, 464 (2004).
- <sup>46</sup>A. Duvenbeck, O. Weingart, V. Buss, and A. Wucher, Nucl. Instrum. Methods Phys. Res. B **255**, 281 (2007).
- <sup>47</sup>A. Duvenbeck, O. Weingart, V. Buss, and A. Wucher, New J. Phys. **9**, 38 (2007).
- <sup>48</sup>A. Duvenbeck, O. Weingart, V. Buss, and A. Wucher, Nucl. Instrum. Methods Phys. Res. B **258**, 83 (2007).
- <sup>49</sup>B. Weidtmann, A. Duvenbeck, and A. Wucher (unpublished).